

UCRL- 92497  
PREPRINT

FURTHER ASSESSMENT OF FEM3 - A NUMERICAL MODEL  
FOR THE DISPERSION OF HEAVY GASES OVER  
COMPLEX TERRAIN

Stevens T. Chan  
Donald L. Ermak

This paper was prepared for submittal to  
the 1985 JANNAF Safety and Environmental  
Protection Subcommittee Meeting,  
Monterey, CA, November 4-8, 1985.

October 1985

Lawrence  
Livermore  
National  
Laboratory

This is a preprint of a paper intended for publication in a journal or proceedings. Since changes may be made before publication, this preprint is made available with the understanding that it will not be cited or reproduced without the permission of the author.

#### **DISCLAIMER**

**This document was prepared as an account of work sponsored by an agency of the United States Government. Neither the United States Government nor the University of California nor any of their employees, makes any warranty, express or implied, or assumes any legal liability or responsibility for the accuracy, completeness, or usefulness of any information, apparatus, product, or process disclosed, or represents that its use would not infringe privately owned rights. Reference herein to any specific commercial products, process, or service by trade name, trademark, manufacturer, or otherwise, does not necessarily constitute or imply its endorsement, recommendation, or favoring by the United States Government or the University of California. The views and opinions of authors expressed herein do not necessarily state or reflect those of the United States Government or the University of California, and shall not be used for advertising or product endorsement purposes.**

FURTHER ASSESSMENT OF FEM3 - A NUMERICAL MODEL  
FOR THE DISPERSION OF HEAVY GASES OVER COMPLEX TERRAIN\*

S.T. Chan and D.L. Ermak  
Lawrence Livermore National Laboratory  
Livermore, California

ABSTRACT

FEM3 is a three-dimensional numerical model for simulating the atmospheric dispersion of heavy gases over complex terrain. During the past few years, FEM3 has been assessed, using data from the Burro and Coyote series of LNG spill experiments conducted by LLNL at China Lake, California. In general, the model has been found to perform very well and it greatly complements the field experiments in enhancing our understanding of the phenomena associated with LNG vapor dispersion, including gravity spreading, heating from the ground surface, and terrain effects. In this paper, the FEM3 model is further applied to simulate the dispersion of nitrogen dioxide ( $\text{NO}_2$ ) for one of the LLNL conducted nitrogen tetroxide ( $\text{N}_2\text{O}_4$ ) spill tests and also to simulate the dispersion of propane gas for four of the refrigerated liquid propane spills conducted by SHELL Research Limited at Maplin Sands. The main purpose of the  $\text{NO}_2$  simulation is to demonstrate the heavy gas effects in this test and the latter simulations are for assessing the performance of the current model for simulating the dispersion of propane gas.

INTRODUCTION

FEM3 is a three-dimensional computer model that was designed to simulate the atmospheric dispersion of large heavier-than-air gas releases [1,2]. The model solves the time-dependent conservation equations of mass, momentum, energy, and species and treats turbulence by use of a K-theory submodel. A generalized anelastic approximation is employed to accommodate large density changes in space and time, and yet preclude sound waves. The model can also handle neutrally buoyant gas releases.

Over the past few years, the results from FEM3 simulations have been compared with the data obtained from a variety of field-scale experiments including liquefied natural gas (LNG), ammonia ( $\text{NH}_3$ ), and nitrogen tetroxide ( $\text{N}_2\text{O}_4$ ) spill tests. All of these were conducted by the Lawrence Livermore National Laboratory under the sponsorship of the U.S. Department of Energy. An early version of FEM3, applied to simulate several of the Burro series experiments, yielded results that correlated quite well with the field data [3]. In particular, the model successfully predicted the bifurcated structure of the vapor cloud in the Burro 8 test, which was conducted under low wind speed and stable atmospheric conditions. Since then, FEM3 has been extended to treat variable terrain, the K-theory turbulence submodel has been improved to account for density stratification and ground heat transfer effects, and new submodels to treat aerosol and humidity effects have been added. With these improvements, additional comparisons were made with the LNG tests, and also the  $\text{NH}_3$  and  $\text{N}_2\text{O}_4$  tests [4-8].

In this paper, we further assess the performance of the FEM3 model in simulating heavier-than-air gas releases. The model results are compared to one of the nitrogen tetroxide spill tests conducted by LLNL [9] and four refrigerated liquid propane spill tests conducted by SHELL Research Limited at Maplin Sands [10,11]. All of these tests involved continuous but finite duration spills of liquid that rapidly evaporated to form a heavier-than-air gas release. The study of dense-gas effects on dispersion in the atmosphere is somewhat complicated by other physical phenomena in the LNG,  $\text{NH}_3$ , and  $\text{N}_2\text{O}_4$  tests due to the very low temperature of LNG, the presence of an ammonia aerosol in the high pressure ammonia tests, and the formation of a nitric acid mist in the  $\text{N}_2\text{O}_4$  tests. The propane experiments allow for the most direct study of dense-gas effects since they do not form an aerosol and the temperature of the liquid ( $\sim 230^\circ\text{K}$ ) is close to ambient temperature thus precluding large heating effects.

MODEL DESCRIPTION

GOVERING EQUATIONS

The FEM3 model is based on solving the following three-dimensional, time-dependent conservation equations:

$$\frac{\partial(\rho u)}{\partial t} + \rho u \cdot \nabla u = -\nabla p + \nabla \cdot (\rho K^m \cdot \nabla u) + (\rho - \rho_h) g, \quad (1)$$

$$\nabla \cdot (\rho u) = 0, \quad (2)$$

\* Work performed under the auspices of the U.S. Dept. of Energy by the Lawrence Livermore National Laboratory (Contract No. W-7405-ENG-48). Approved for public release; distribution is unlimited.

$$\frac{\partial \theta}{\partial t} + \underline{u} \cdot \nabla \theta = \frac{1}{\rho C_p} \nabla \cdot (\rho C_p \underline{K}^\theta \cdot \nabla \theta) + \frac{C_{PN} - C_{PA}}{C_p} (\underline{K}^\omega \cdot \nabla \omega) \cdot \nabla \theta, \quad (3)$$

$$\frac{\partial \omega}{\partial t} + \underline{u} \cdot \nabla \omega = \frac{1}{\rho} \nabla \cdot (\rho \underline{K}^\omega \cdot \nabla \omega), \quad (4)$$

and

$$\rho = \frac{PM}{RT} = \frac{P}{RT \left( \frac{\omega}{M_N} + \frac{1-\omega}{M_A} \right)}, \quad (5)$$

$$C_p = C_{pA} + (C_{pN} - C_{pA})\omega, \quad (6)$$

where  $\underline{u} = (u, v, w)$  is the velocity,  $\rho$  is the density of the mixture,  $p$  is the pressure deviation from an adiabatic atmosphere at rest, with corresponding density  $\rho_h$ ,  $\underline{g}$  is the acceleration due to gravity,  $\theta$  is the potential temperature deviation from an adiabatic atmosphere at  $\theta_0$ ,  $\omega$  is the mass fraction of the dispersed species,  $\underline{K}^m$ ,  $\underline{K}^\theta$ , and  $\underline{K}^\omega$  are the eddy diffusion tensors for momentum, energy, and the dispersed species,  $C_{pN}$ ,  $C_{pA}$ , and  $C_p$  are the specific heats for the species, air, and the mixture, respectively. In the equation of state,  $P$  is the absolute pressure,  $R$  is the universal gas constant,  $M_N$ ,  $M_A$  are the molecular weights of the species and air, and  $T$  is the absolute temperature ( $T/(\theta + \theta_0) = (P/P_0)^{R/MC_p}$ ). For problems of current interest, because the heights of interest are generally small ( $\ll 1$  km), the ratio  $P/P_0$  is nearly equal to unity and hence no distinction is made between the absolute and potential temperature. Details of the model can be found in [1] and the numerical techniques employed are described in [2]. Herein we only discuss briefly the treatment of the vapor source and the turbulence submodel.

#### VAPOR SOURCE

The source of the dispersing cloud is basically defined by injecting an appropriate amount of mass and energy through a predetermined source area (usually on the ground). During vapor injection, the following boundary conditions are imposed:

$$V = V_I \quad \text{for the vertical momentum equation,} \quad (7)$$

and

$$K_v \frac{\partial \omega}{\partial n} = \frac{V_I}{\rho} (1-\omega) \quad \text{for the species equation,} \quad (8)$$

where  $V_I = (\rho v)_I$  is the mass flux of the vapor being injected. For the temperature equation, consideration of enthalpy balance leads to (see [8]):

$$K_v \frac{\partial \theta}{\partial n} = \frac{V_I}{\rho} \left( \frac{C_{pN}}{C_p} \theta_N - \theta \right). \quad (9)$$

A refined numerical treatment of the vapor source is contained in Appendix A.

#### TURBULENCE SUBMODEL

In the present model, the eddy diffusion tensors  $\underline{K}^m$ ,  $\underline{K}^\theta$ , and  $\underline{K}^\omega$  are assumed to be diagonal and it is further assumed that  $\underline{K}^\theta = \underline{K}^\omega$ . The vertical and horizontal diffusion coefficients are given respectively by:

$$K_v = \frac{k [(u_* z)^2 + (w_* z)^2]^{1/2}}{\phi} \quad (10)$$

and

$$K_h = \beta k u_* z / \phi \quad (11)$$

In the above equations,  $u_*$  is the local "friction velocity" incorporating the effects of the ambient and the resulting velocity field,  $w_*$  is the "convection velocity" due to ground heating of the vapor cloud, and  $\phi$  is the Monin-Obukhov profile function given by Dyer [12]. Specifically,  $\phi$  is defined as

$$\phi = 1 + 5 Ri, \quad Ri \geq 0 \quad (12a)$$

for all three (momentum, energy, and species) diffusion coefficients, and

$$\phi = \begin{cases} (1 - 16 Ri)^{-1/4} & \text{for momentum,} \\ (1 - 16 Ri)^{-1/2} & \text{for energy and species.} \end{cases} \quad Ri \leq 0 \quad (12b)$$

The local Richardson number is, in turn, defined as

$$Ri = u_*^2 \frac{Ri_a}{(u_*^2 + w_*^2)} + 0.05 \frac{(\rho - \rho_a)}{\rho} \cdot \frac{gk}{(u_*^2 + w_*^2)} \quad (13)$$

Herein the first term is designed to include the turbulence in the ambient atmosphere and the second term represents the effects of density stratification, generally a reduction of turbulence in the stably stratified, dense vapor cloud.  $Ri_a$  and  $\rho_a$  are the Richardson number and density of the ambient atmosphere. The ambient density is obtained via equation (5) and the ambient Richardson number is defined as

$$Ri_a = z/L \quad (14)$$

where  $z$  is the height above ground and  $L$  is the Monin-Obukhov length scale.

#### MODEL-DATA COMPARISONS

In the following, we compare the FEM3 results with data obtained in five selected field tests. Table 1 summarizes the spill and atmospheric conditions for these tests. The scarcity of measured data in the  $N_2O_4$  tests and the uncertainties in the source strength significantly limit the usefulness of these tests for model validation. The main purpose for this comparison is to demonstrate the presence of heavy gas dispersion effects in this test. For the SHELL tests, sufficient data is available for more quantitative comparison.

Table I. Spill and Atmospheric Conditions

Parameters	Trials SHELL 47	SHELL 49	SHELL 50	SHELL 54	LLNL Eagle 3
Spill Rate ( $m^3/min$ ) (Kg/s)	3.9 37.6	2.1 20.3	4.3 41.5	2.3 22.2	0.283 6.83
Simulated Spill Duration (s)	120	120	120	180	600
Wind Sped @ 10m (m/s)	5.6±0.6	6.2±0.5	7.9±0.9	3.8±0.3	3.66
Friction Velocity (m/s)	0.19	0.21	0.27	0.13	0.12
Ambient Monin-Obukhov Length Scale (m)	520	64.3	201	83.5	23.2
Momentum Diffusivity @ 1m ( $m^2/s$ )	0.0753	0.0779	0.1054	0.0491	0.0401
Release Richardson No. $Ri_0$	35	18	13	90	9

All of the simulated results presented herein were obtained with graded meshes, each consisting of 4653 mesh points (9 x 11 x 47). A plane of symmetry along the mean wind direction was assumed for all the cases. The computational domain containing half of the vapor cloud (with the origin of the coordinates placed at the spill point) extends from  $x = -100$  to 1100 m,  $y = 0$  to 120 m,  $z = 0$  to 35 m for Eagle 3, and is from  $x = -90$  to 600 m (520 m for SHELL 54),  $y = 0$  to 75 m, and  $z = 0$  to 10 m for the SHELL simulations. On the upwind surface, a parabolic wind profile, fitted with measured data at  $z = 1$  m (or  $z = 2$  m for Eagle 3) and 10 m, together with zero slope vertically at  $z = 10$  m, was specified. Heat transfer from the ground or water surface was included in all simulations and, unless noted otherwise, an effective energy transfer velocity of 0.0125 m/s was used.

### EAGLE 3

This test was conducted under relatively low wind speed and stable atmospheric conditions [9]. During the test, liquid nitrogen tetroxide ( $N_2O_4$ ) was spilled directly onto the ground, which then quickly evaporated and became nitrogen dioxide ( $NO_2$ ). As discussed by McRae, the exact source strength of  $NO_2$  was difficult to determine owing to two main reasons: (1) in the source area, a certain amount of liquid  $N_2O_4$  permeated directly onto the ground, and (2) during vapor dispersion, some of the  $NO_2$  reacted with water vapor in the air and formed a nitric acid ( $HNO_3$ ) mist. In the numerical simulations, the equivalent source rate of  $NO_2$  was taken to be 410 Kg/min based on McRae's best estimate, and the source area was assumed to be 20 m x 20 m.

In order to demonstrate the heavy gas effects, the dispersed gas was treated as both a heavy gas ( $NO_2$ ) and a neutral gas (air). A sample of the predicted results are shown in Figs. 1 and 2. The heavy gas effects are shown clearly in Fig. 1 for the crosswind plane at 800 m from the source. For instance, the 100 ppm contour in the heavy gas case is much lower (16 m vs 20 m) and wider (180 m vs 140 m for the entire cloud width). In Fig. 2, the predicted maximum concentrations along the mean wind direction at 1-m high are compared. The heavy gas curve is below the neutral gas curve (for  $x > 35$  m) but the two are approaching a common slope in the far field. The fact that the heavy gas case has lower concentration is due to the significant gravity spreading which, through its density-gradient induced vortices, entrains air through its widened top surface to dilute the vapor cloud. Opposing this enhanced dilution effect, the stable density stratification within the cloud tends to reduce turbulent mixing and cloud dilution. However, this competing effect has been found to be generally weaker than the former mechanism when the ambient atmospheric condition is stable [8]. Also shown in Fig. 2 is the estimated range of concentration from the field data at  $x = 785$  m. The  $NO_2$  concentration was measured to be above 500 ppm (saturated sensor), and based on the source strength estimates, an upper bound of 2275 ppm was considered to be more appropriate. With the uncertainties in source strength taken into account, the predicted concentration at this location appears to be quite reasonable.

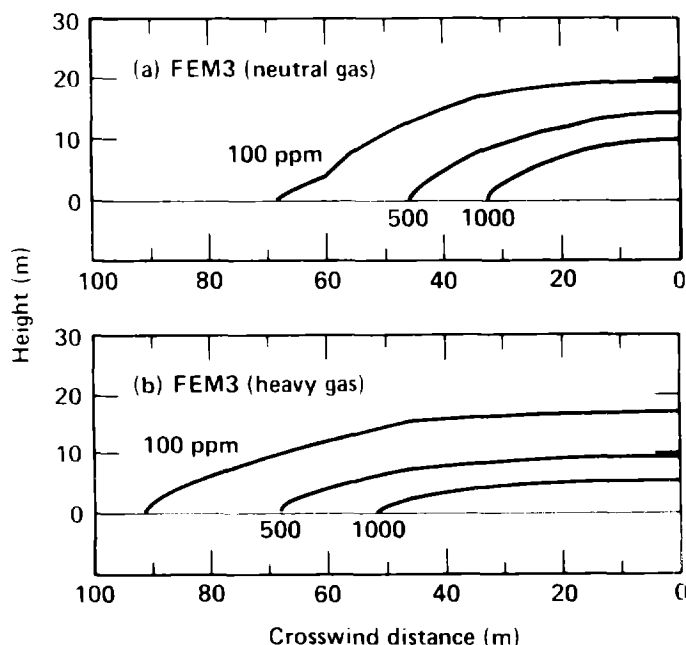


Fig. 1. Eagle 3  $NO_2$  concentration contours 800 m downwind at  $t = 360$  s: (a) neutral gas, (b) heavy gas.

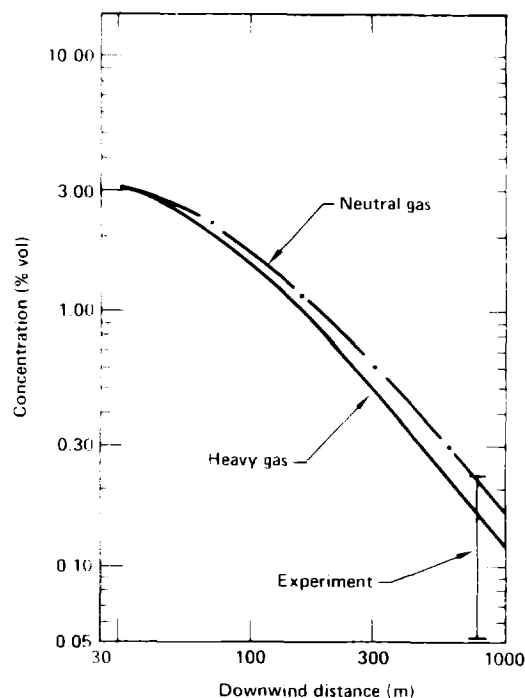


Fig. 2. Eagle 3 maximum  $NO_2$  concentration versus downwind distance.

## SHELL PROPANE SPILLS

Four continuous propane spills, Nos. 47, 49, 50, and 54, were simulated. Due to space limitations, only one type of comparison will be presented for the first three tests. The experimental peak concentration values will be compared with the maximum, center plane concentrations predicted by the model. The recorded concentration data were averaged using a three-second average and the peak values were determined from all available time-series of concentration data at the same distance from the source, irrespective of the angular position and times. For Spill 54, concentration contours on a few selected planes are also included to illustrate the general features of a propane vapor cloud under low wind conditions.

FEM3, like most numerical models, calculates only an ensemble-averaged concentration. Also, the meteorological and spill conditions (except when the vapor source is terminated) are assumed to be constant in time. Thus the typical time-series of predicted concentration look like those depicted in Fig. 3, which are relatively smooth, and only systematic cloud structures (including gravity waves) are reflected. On the other hand, the observed concentrations in an experiment generally contain many higher frequency random components, as shown in Fig. 4. These numerous peaks and valleys are due to a number of reasons, including turbulence in the ambient atmosphere (large-scale turbulence would cause cloud meander), turbulence induced by the cloud (such as density-gradient-induced vortices), nonuniformity of source rate, and possibly shear instabilities on the cloud/air interface. As most of these effects are either excluded or can only be approximately modeled, relatively large discrepancies between data and the numerical predictions can be expected. This may be especially true for Spill 49, which has a short spill duration ( $\sim 90$  s) and less uniform spill rate. The model-data comparisons are summarized in Figs. 5 through 9.

As is seen in Fig. 5, for Spill 47, the agreement for concentration at  $z = 0.9$  m is very good. At  $z = 2.3$  m, there is significant scatter in the experimental data, however, the general trend is well-predicted. For the temperature field, at  $x = 135$  m from the source and at  $z = 0.9$  m, FEM3 predicts a drop of about 3.5 degrees, which is in fair agreement with the observed temperature drop of 2 to 3 degrees. Furthermore, FEM3 predicts a visible cloud (which corresponds to  $\sim 2.6\%$  concentration assuming adiabatic mixing) of approximately 60 m wide and 240 m long, compared with about 70 m x 210 m from the photographic data.

Heat transfer effects from the sea surface on the cloud were also investigated for this case. To do so, the temperature on the lower boundary (except for the source area over which enthalpy balance was imposed) was set equal to the sea surface temperature to allow for maximum heat transfer into the cloud. At  $z = 0.9$  m, the cloud was warmer by up to a couple of degrees; however, the concentration field changed only slightly, generally less than 5% in relative values compared to the previous simulation. Thus, unlike LNG, heat transfer from the surface does not seem to be playing a very important role in the dispersion of a propane plume.

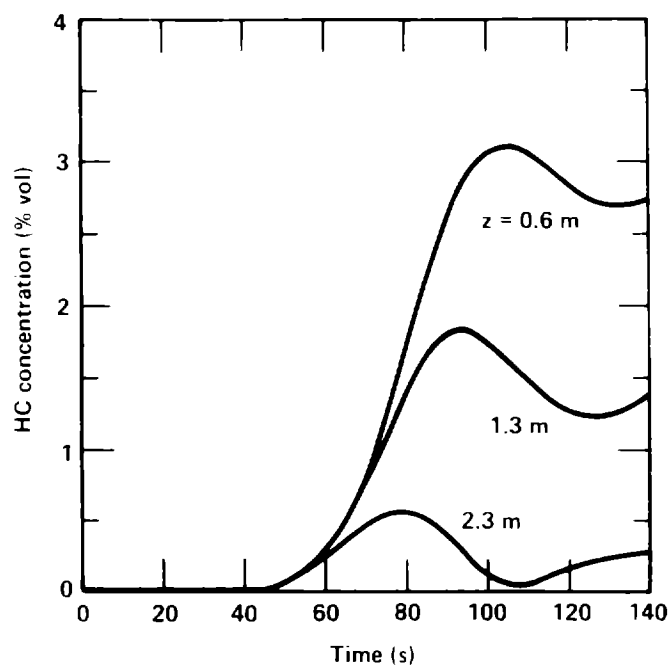


Fig. 3. Predicted time-series of HC concentration at 180 m from the source of LPG Spill 54.

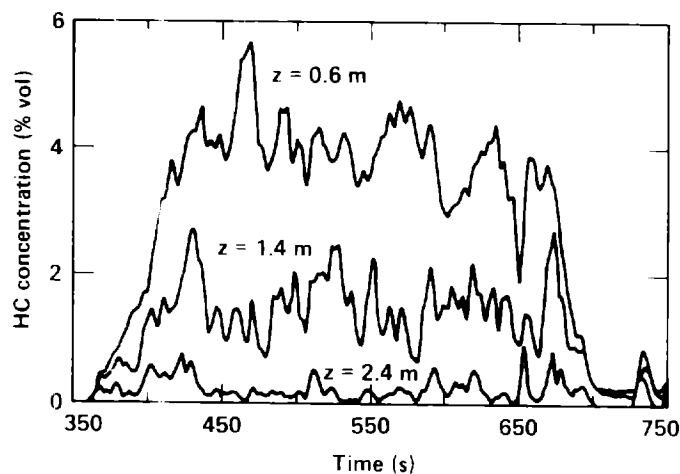


Fig. 4. Measured time-series of HC concentration at 180 m from the source of LPG Spill 54 (spill starts at  $t=300$  s).

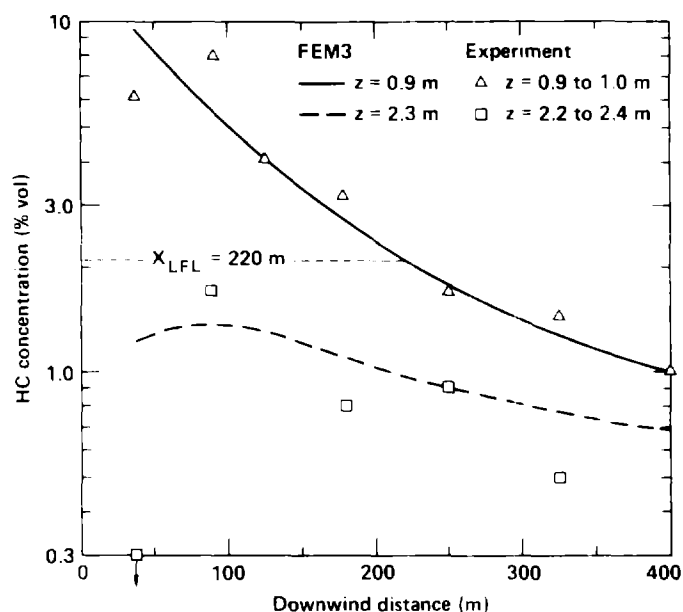


Fig. 5. Comparison of predicted maximum concentrations versus measured peak values for LPG Spill 47.

The data and predicted maximum concentrations for Spill 49 are plotted in Fig. 6. As is seen, the agreement at  $z = 2.3$  m is fairly good; however, large differences (a factor of 2 or slightly more) exist at  $z = 0.9$  m. A close examination of the time-series of concentration data reveals a strong peak about 70 seconds after the arrival of gas at each sensor location, which thus set the peak values of the measured data. Such an anomaly, based on the SHELL data report, is probably due to one or more of the following reasons: (1) the flow rate was uncontrolled for more than half of the spill period; (2) the wind was not very homogeneous; and (3) the duration of constant spill was short. Considering the fact that the present test was conducted at a slightly higher wind speed than Spill 47 and with only about half the spill rate, the observed peak values of concentration appear to be too high for the recorded average spill and meteorological conditions. It is possible that a sizable puff of cloud was generated, due to one or a combination of the aforementioned reasons, thus creating the strong peak on most of the sensors. For the temperature field, FEM3 predicts a temperature drop of approximately 2 degrees at  $z = 0.9$  m and 135 m from the source, compared to a drop of 2 to 3 degrees at  $z = 0.7$  m in the experiment. The visible cloud predicted by the code (1.75% concentration) is approximately 40 m wide and 230 m long, as compared with 60 m and 180 m from the photographic data.

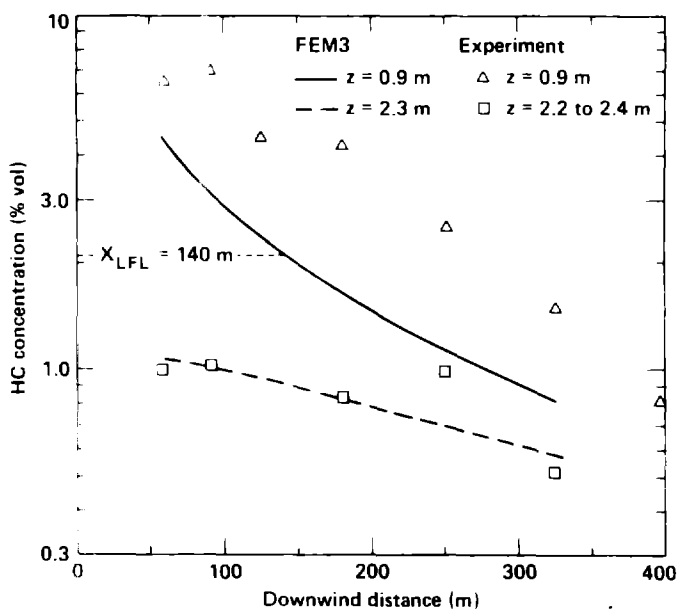


Fig. 6. Comparison of predicted maximum concentrations versus measured peak values for LPG Spill 49.

Compared to Trial 47, Trial 50 has a slightly higher spill rate (4.3 vs 3.9 m<sup>3</sup>/min) and a much higher wind speed (7.9 vs 5.6 m/s). The predicted maximum concentrations on the center plane are compared with the measured data in Fig. 7. Except for the data at  $x = 130$  m and  $z = 2.3$  m, the overall agreement between model predictions and field measurements is remarkably good. Such good agreement is probably attributable to the closeness of the field conditions and the simulated conditions. In particular, this test has fairly steady spill and meteorological conditions, including a well-controlled flow rate, a relatively long period of steady spill, and a fairly steady and homogenous wind velocity. For the temperature field, FEM3 predicts a temperature drop of approximately 4 degrees at  $x = 90$  m and a drop of about 2 degrees at  $x = 180$  m (for  $z = 0.9$  m high), both appear to agree well with the data. The predicted visible cloud (3.2% concentration) of approximately 40 m by 190 m is also close to the cloud size of 50 m by 180 m based on photographic data.

Spill 54 has the lowest wind speed of all the simulated spills. Its plume was wider than all the other cases and shows clearly the effects of gravity spreading from the source region onwards. Simulated results for this case are shown in Figs. 8 through 11. Results in Fig. 8 were obtained using a friction velocity of  $U_* = 0.034 U_{10}$ . As is seen in the figure, the predicted concentrations imply too high a vapor cloud. As an attempt to resolve this discrepancy, a finer mesh consisting of 9180 nodal points (12 x 15 x 51) was also used for the simulation. However, predicted concentrations changed only a few percent (in relative values) from the coarse mesh solution, implying that the coarse mesh solution is nearly mesh convergent. A preliminary investigation reveals that our current turbulence submodel tends to underestimate the cloud height and does not seem to have sufficient turbulence damping for the upper part of the vapor cloud. This potential deficiency is especially severe for cases where the plume is very low (~1 m high). As a quick fix and alternative to a more sophisticated turbulence submodel, we reduced the value of the friction velocity by a factor of three, and the simulated results are shown in Fig. 9. Although relatively large discrepancies still exist in the far field, the agreement between model predictions and measured data is much better. Figures 10 and 11 show respectively the vertical profile of the shallow plume and the shapes of the plume at several heights. Overall, the predicted results are in agreement with observation of a cloud being about 1 to 1 1/2 m high. The predicted visible cloud (3.1.8% concentration) is about 100 m wide and 275 m long, as compared to approximately 110 m by 260 m from the photographic data. The predicted temperature drop at 58 m from the source and  $z = 0.6$  m is about 4.5 degrees, compared to a drop of about 2 to 4 degrees at  $z = 0.7$  m in the experiment.

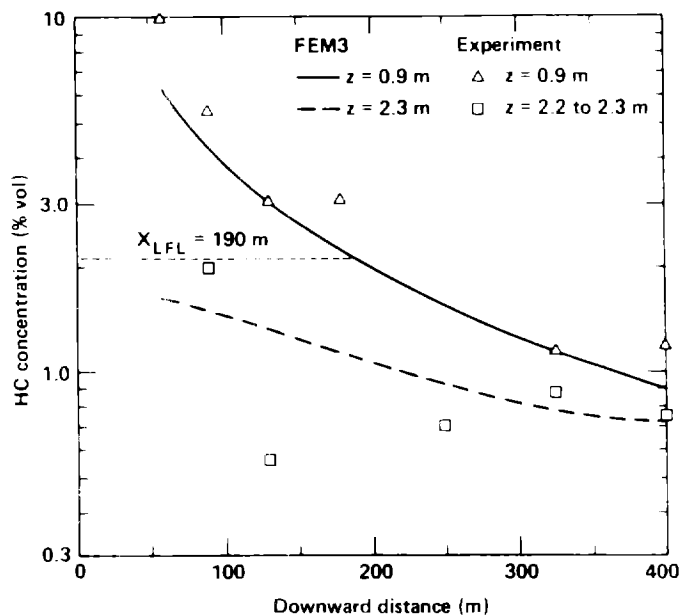


Fig. 7. Comparison of predicted maximum concentrations versus measured peak values for LPG Spill 50.

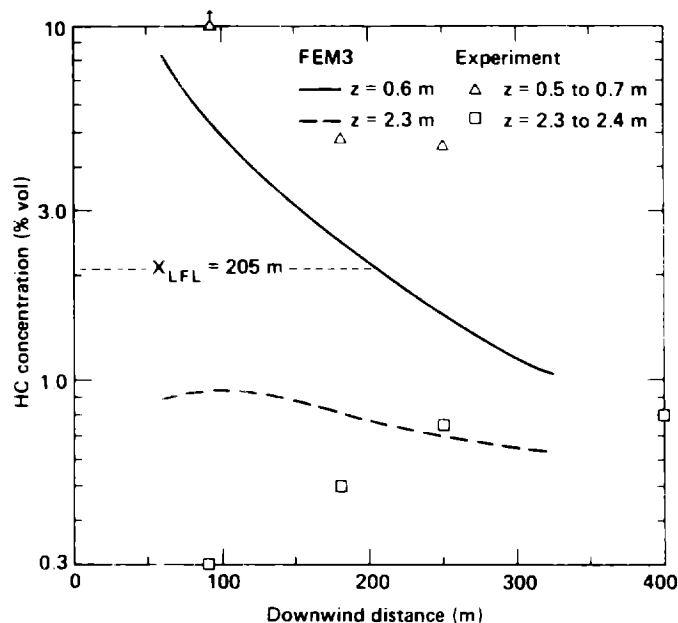


Fig. 8. Comparison of predicted maximum concentrations versus measured peak values for LPG Spill 54 ( $U_* = 0.129$  m/s in calculations).

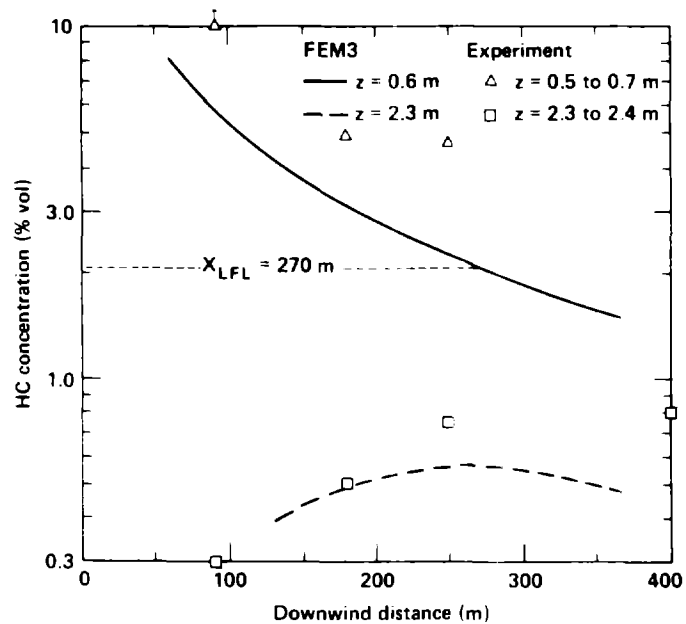


Fig. 9. Comparison of predicted maximum concentrations versus measured peak values for LPG Spill 54. ( $u_* = 0.043 \text{ m}^2/\text{s}$  in calculations).

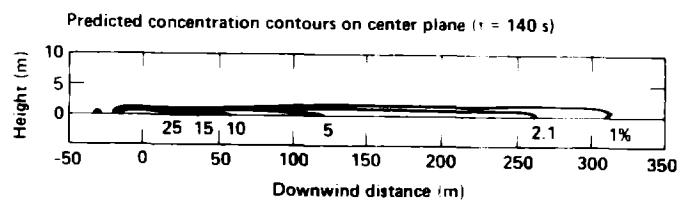


Fig. 10. Predicted concentration contours on center plane for LPG Spill 54 at  $t = 140 \text{ s}$ . (Vertical to horizontal distance scale is 1 to 4)

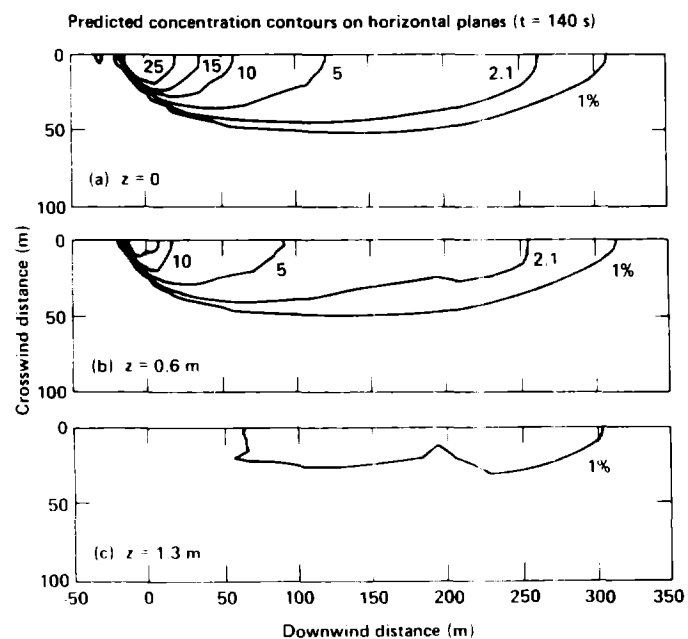


Fig. 11. Predicted concentration contours on various horizontal planes for LPG Spill 54 at  $t = 140 \text{ s}$ .

In Fig. 12, the predicted downwind distance to the lower flammability limit,  $X_{LFL}$ , are plotted and compared with field data, together with estimates of uncertainties. The ratios between data and model prediction for the values of  $X_{LFL}$  are 1.07, 2.04, 1.11, and 1.67 for Spills 47, 49, 50, and 54, respectively.

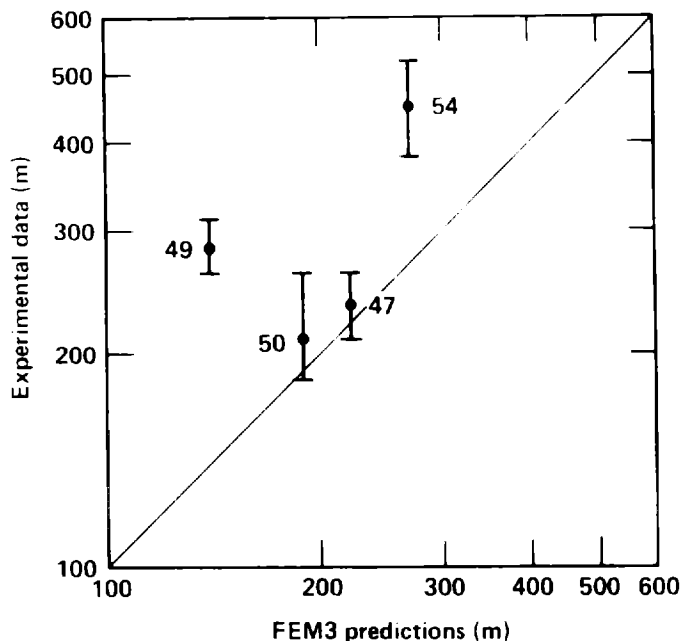


Fig. 12 Calculated versus experimental values of downwind distance to the LFL for four selected LPG spill tests.

#### SUMMARY AND CONCLUSIONS

In this paper, FEM3 has been applied to simulate the vapor dispersion of  $\text{NO}_2$  and propane gas releases. In general, good agreement between model predictions and field data was observed. For SHELL propane Spills 49 and 54, larger discrepancies exist and are probably due to the greater variability in the experimental conditions (vs constant conditions as assumed in the numerical simulation) in Spill 49 and due to inaccurate parameterization of turbulence in Spill 54, where an extremely low vapor cloud was produced.

In the propane plume simulations, heat transfer from the sea surface was found to be relatively unimportant, compared to other effects such as spill rate and atmospheric turbulence. Apparently this is due to the fact that the boiling temperature of refrigerated liquid propane is not too far below the ambient temperature.

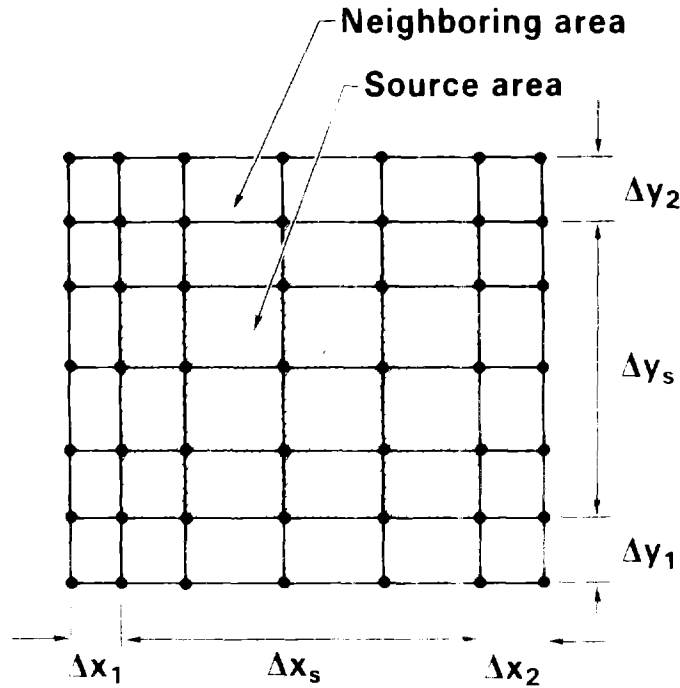
In the  $\text{NO}_2$  dispersion simulations, it was demonstrated that significant heavy gas effects exist even for a spill rate as low as  $\sim 7 \text{ Kg/s}$ . In general, with heavy gas effects considered, the hazardous region is much wider than that corresponding to a neutrally buoyant gas cloud, although the downwind extent of such a region may be somewhat shorter under stable atmospheric conditions.

# REFERENCES

1. S.T. Chan, FEM3 -- A Finite Element Model for the Simulation of Heavy Gas Dispersion and Incompressible Flow: User's Manual, UCRL-53397, Lawrence Livermore National Laboratory, Livermore, CA, 1983.
2. P.M. Gresho, S.T. Chan, R.L. Lee, and C.D. Upson, "A Modified Finite Element Method for Solving the Time-Dependent, Incompressible Navier-Stokes Equations," Int. J. Num. Meth. Fluids, 4, Part 1: Theory, 557-598; Part 2: Applications, 619-640, 1984.
3. D.L. Ermak, S.T. Chan, D.L. Morgan, and L.K. Morris, "A Comparison of Dense Gas Dispersion Model Simulations with Burro Series LNG Spill Test Results," J. of Haz. Mat., 1982, Vol. 6, pp. 129-160, Nos. 1 and 2, also in Dense Gas Dispersion, Elsevier Scientific Publishing Co., Amsterdam, 1982.
4. S.T. Chan, H.C. Rodean, and D.L. Ermak, "Numerical Simulations of Atmospheric Releases of Heavy Gases Over Variable Terrain," Air Pollution Modeling and its Application III, Plenum Press, 295-341, 1984.
5. S.T. Chan, and D.L. Ermak, "Recent Results in Simulating LNG Vapor Dispersion over Variable Terrain," Atmospheric Dispersion of Heavy Gases and Small Particles, Springer-Verlag, 105-114, 1984.
6. D.L. Ermak, S.T. Chan, and E.J. Kansa, Denser-Than-Air Dispersion Modeling in the Atmosphere, presented at the JANNAF Safety & Environmental Protection Subcommittee Meeting, March 1983.
7. E.J. Kansa, D.L. Ermak, S.T. Chan, and H.C. Rodean, Atmospheric Dispersion of Ammonia: An Ammonia Fog Model, proceedings of the Multiphase Synfuels Heat Transfer 21st ASME/AIChE National Heat Transfer Conference, Seattle, WA, July 24- 28, 1983.
8. D.L. Ermak, and S.T. Chan, A Study of Heavy Gas Effects on the Atmospheric Dispersion of Dense Gases, proceedings of the 15th International Technical Meeting on Air Pollution Modeling and its Application, St. Louis, MO, April 15-19, 1985.
9. T.G. McRae, Analysis and Model/Data Comparisons of Large-Scale Releases of Nitrogen Tetroxide, Lawrence Livermore National Laboratory, Livermore, CA, UCID-20388, March 1985.
10. J.S. Puttock, G.W. Colenbrauder, and D.R. Blackmore, "Maplin Sands Experiments 1980: Dispersion Results from Continuous Releases of Refrigerated Liquid Propane, " Heavy Gas and Risk Assessment - II, D. Reidel Publ. Co., 147-161, 1982.
11. G.W. Colenbrander, A.E. Evans, and J.S. Puttock, Spill Tests of LNG and Refrigerated Liquid Propane on the Sea, Maplin Sands, 1980: Dispersion Data Digests, Shell Thornton Research Center, May 1984.
12. A.J. Dyer, "A Review of Flux-Profile Relationships," Boundary-Layer Met., 7, 363-372, 1974.

# APPENDIX A - NUMERICAL TREATMENT OF VAPOR SOURCE

Equations (7) through (9) are valid for the continuum. In a numerical approach, however, due to the use of finite grid spacings and the nature of using piecewise polynomial approximation for the variables being solved, direct application of these equations over all the grid points covering the source will often result in too much material being injected, especially when the neighboring area outside of the source is not small compared to the source area (see sketch below). To obtain a more accurate injection rate, we introduce a correction factor for the value of  $V_I$ .



Sketch showing the source area and its neighboring area.

Let us consider a two-dimensional case, for which vapor is being injected over  $\Delta X_s$ . The vapor injection rate is

$$\dot{m}_s = (\rho v)_I \cdot \omega \cdot \Delta X_s = V_I \Delta X_s,$$

noting that  $\omega = 1$  over the source (this is not to be confused with the grid point value, which is being computed and can not exceed 1). However, due to space discretization errors, an additional amount of vapor is injected over the neighboring upwind and downwind grid spacings,

$$\dot{m}_a = \int_{\Delta X_1} (\rho v) \omega dx + \int_{\Delta X_2} (\rho v) \omega dx.$$

With the piecewise linear approximation currently employed for  $\rho v$  and  $\omega$ , whose values are equal to  $V_I$  and 1 over the edges of the source and diminish to 0 at the neighboring nodes, the above integrals lead to

$$\dot{m}_a = V_I (\Delta X_1 + \Delta X_2) / 3.$$

Thus, the actual material injection rate is

$$\dot{m} = \dot{m}_s + \dot{m}_a = V_I [\Delta X_s + (\Delta X_1 + \Delta X_2) / 3].$$

Therefore, in order to yield the desired injection rate,  $V_I \Delta X_s$ , a correction factor should be applied to the value of  $V_I$  as

$$f_{2D} = \frac{\Delta X_s}{\Delta X_s + (\Delta X_1 + \Delta X_2)/3} \quad (A-1)$$

Similarly, for injection over an area, the correction factor is

$$f_{3D} = \frac{\Delta X_s \Delta Y_s}{[\Delta X_s + (\Delta X_1 + \Delta X_2)/3][\Delta Y_s + (\Delta Y_1 + \Delta Y_2)/3]} \quad (A-2)$$

For uniform mesh,  $\Delta X_1 = \Delta X_2 = \Delta X$ ,  $\Delta X_s = m\Delta X$ ,  $\Delta Y_1 = \Delta Y_2 = \Delta Y$ ,  $\Delta Y_s = n\Delta Y$ , the above equations reduce to

$$f_{2D} = \frac{3m}{3m + 2} \quad (A-3)$$

and

$$f_{3D} = \frac{9mn}{(3m + 2)(3n + 2)} \quad (A-4)$$